



# Observational Study of Reynolds Stresses Associated with Solar Inertial Modes

Yash Mandowara<sup>1</sup> , Yuto Bekki<sup>1</sup>, Richard S. Bogart<sup>2</sup> and Laurent Gizon<sup>1,3</sup> 

<sup>1</sup>Max-Planck-Institut für Sonnensystemforschung, 37077 Göttingen, Germany  
email: [yash.uni13n@gmail.com](mailto:yash.uni13n@gmail.com)

<sup>2</sup>Stanford University, Stanford, CA 94305-4085, USA

<sup>3</sup>Institut für Astrophysik, Georg-August-Universität Göttingen, 37077 Göttingen, Germany

**Abstract.** We study the  $m = 1$  high-latitude inertial mode and its contribution to the latitudinal transport of the Sun's angular momentum. Ring-diagram helioseismology applied to  $5^\circ$  tiles is used to obtain the horizontal flows near the surface of the Sun. Using 10 years of data from SDO/HMI, we report on the horizontal eigenfunction and Reynolds stress  $Q_{\theta\phi} = \langle u'_\theta u'_\phi \rangle$  for the  $m = 1$  high-latitude inertial mode (frequency  $-86.3$  nHz, critical latitudes  $\pm 58^\circ$ ). We find that  $Q_{\theta\phi}$  takes significant values above the critical latitude and is positive (negative) in the northern (southern) hemisphere, implying equatorward transport of angular momentum. The  $Q_{\theta\phi}$  peaks above latitude  $70^\circ$  with a value of  $38 \text{ m}^2/\text{s}^2$ .

**Keywords.** Solar inertial modes, solar oscillations, helioseismology, solar rotation

---

## 1. Introduction

Inertial modes are low-frequency modes of global oscillations whose restoring force is the Coriolis force. Although inertial modes were predicted to exist in the Sun since 1970s, they were only recently detected on the Sun. Using 10 years of data from SDO/HMI, Löptien et al. (2018) unambiguously detected the equatorial Rossby modes, a particular class of quasi-toroidal inertial modes. Gizon et al. (2021) further detected and identified a large number of additional modes at middle and high latitudes in the inertial frequency range. The modes were identified with the help of a linear eigenmode solver (Bekki et al. 2022a). More recently Hanson et al. (2022) also reported another family of inertial modes on the Sun.

All of these observed modes propagate in the retrograde direction (opposite to rotation) when seen from the Carrington frame of reference. For these modes, the Sun's latitudinal differential rotation plays a critical role as it introduces critical latitudes where the phase speed of the mode is equal to the local differential rotation speed (Gizon et al. 2020). Theoretical studies suggest that the inertial modes have substantial Reynolds stresses near the critical latitudes (Gizon et al. 2020; Bekki et al. 2022a,b). Theory also shows that the  $m = 1$  mode is linearly unstable to the sharp latitudinal gradient of rotation at high latitudes (Fournier et al. 2022) and to the associated latitudinal entropy gradient (Bekki et al. 2022a) — this explains why it has a large velocity amplitude (Gizon et al. 2021).

In this study, we report the observational measurement of the horizontal Reynolds stresses associated with  $m = 1$  high-latitude mode, which has the largest velocity amplitude among all the observed solar inertial modes. This will help us to assess the

contribution from the observed inertial modes to the latitudinal transport of the angular momentum of the Sun.

## 2. Methods

### 2.1. Data

In this study, we use ring-diagram local helioseismology (Hill 1988) to obtain the near-surface flow maps of the Sun. The Dopplergrams are obtained from the Helioseismic and Magnetic Imager (HMI) onboard the Solar Dynamics Observatory (SDO). The ring-diagram method involves computing 3D  $(k_x, k_y, \omega)$  local power spectra from small patches (tiles) on the solar surface. Here, we use the highest-resolution ring-diagram data with tile size of  $5^\circ$ , which covers the latitudinal range from  $85^\circ$  N to  $85^\circ$  S (Bogart *et al.* 2011a,b, 2015). The flows near the surface cause Doppler shifts in the f- and p-mode frequencies in the local power spectrum. Fitting for these shifts and averaging the fitted parameters from lower to upper turning points gives the underlying horizontal flows.

Due to lack of sufficient usable data at higher latitudes, we use a cropped version of this data cube, focusing on latitudes  $75^\circ$  N to  $75^\circ$  S. We use a 10-year-long data set from May 2010 to Feb 2021 with a temporal cadence of 9.08 hr (1/72 of the Carrington rotation period). This results in a data cube with  $N_t \times N_\theta \times N_\phi = 10418 \times 61 \times 144$  grid points. The flow maps consist of the longitudinal velocity  $u_x$  and the latitudinal velocity  $u_y$ , both as functions of time  $t$ , colatitude  $\theta$ , and longitude  $\phi$ .

After removing outliers, we remove the systematic effects due to the  $B_0$  angle by modeling it as a harmonic signal with a one-year period. This gives us flow maps free of the most significant systematic errors.

### 2.2. Mode analysis

In contrast to the analysis of Gizon *et al.* (2021), we do not perform north-south symmetrization of flow maps for mode extraction. The HMI ring-diagram products  $(u_x, u_y)$  can be easily converted to standard  $(u_\theta, u_\phi)$  in spherical coordinate,

$$u_\theta = -u_y, \quad u_\phi = u_x. \quad (1)$$

From the processed data above, we generate a power spectrum by performing the Fourier transform in time and longitude:

$$j \in \{\theta, \phi\}, \quad \hat{u}_j(\theta, \nu) = \frac{1}{f(\theta)} \sum_t \sum_\phi u_j(\theta, \phi, t) e^{i(2\pi\nu t - m\phi)}, \quad (2)$$

where  $\nu$  and  $m = 1$  are the frequency and the azimuthal order, respectively, and  $f(\theta)$  is a correction for missing data,

$$f(\theta) = \frac{\text{No. of measurements available at fixed } \theta}{\text{total number of points at fixed } \theta}. \quad (3)$$

### 2.3. Extraction of eigenfunctions

To filter out a mode identified by its azimuthal order  $m$  and peak frequency  $\nu_0$ , we apply a rectangular filter ‘rect’ is unity in the range  $[\nu_0 - \gamma, \nu_0 + \gamma]$  and zero elsewhere, and  $\gamma$  is the FWHM of the line profile of the mode in the power spectrum. This mode has a peak frequency and line-width of  $-86.3$  nHz and  $7.8$  nHz, respectively, and can be seen clearly in the power spectrum of longitudinal velocity  $u_\phi$  (Gizon *et al.* 2021, see Table A.1 therein). To obtain the filtered data in the time domain we apply an inverse

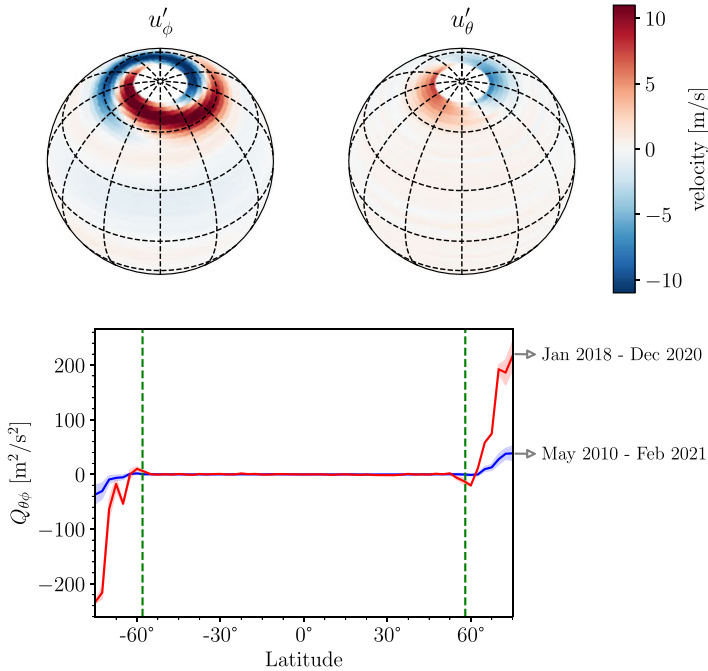


**Figure 1.** Observed velocity eigenfunctions and horizontal Reynolds stress of the  $m = 1$  high-latitude mode (frequency:  $-86.3$  nHz, critical latitude:  $58^\circ$ ). The eigenfunctions are obtained from 10 years of SDO/HMI  $5^\circ$  ring-diagram data. Bottom panel: Reynolds stress  $Q_{\theta\phi}$  during the entire observation period 2010–2021 (blue curve) and during the quiet sun period 2018–2020 (red curve). The green dashed lines mark the critical latitudes for this mode.

Fourier transform in time,

$$U_{qp}^j = \frac{1}{N_t} \sum_{\nu} \hat{u}_j(\theta_p, \nu) \text{rect} \left( \frac{\nu - \nu_0}{\gamma} \right) e^{-2i\pi\nu t_q}, \quad p = 1, \dots, N_\theta, \quad q = 1, \dots, N_t. \quad (4)$$

Next we compute the SVD of the matrix  $[U^\theta \ U^\phi] \in \mathbb{C}^{N_t \times 2N_\theta}$  and retain only one term in the sum,  $s_1 w [v_\theta^H \ v_\phi^H]$ , where  $s_1$  is the largest singular value and the vectors  $w \in \mathbb{C}^{N_t}$  and  $v_j \in \mathbb{C}^{N_\theta}$  are the corresponding singular vectors. The superscript  $H$  denotes the conjugate transpose. The vectors  $v_\theta$  and  $v_\phi$  encapsulate the  $\theta$ -dependence of the mode eigenfunctions. Finally, we normalize the eigenfunctions by the factor  $K$ , such that  $u'_j(\theta, \phi)$  is the effective root mean square representation of the velocity profile of the mode.

$$u'_j(\theta, \phi) := \Re \{ K s_1 v_j^*(\theta) e^{im\phi} \}, \quad K = 2N_\theta^{-1} N_t^{-1/2}. \quad (5)$$

To obtain the latitudinal profile of the horizontal Reynolds stress we compute

$$Q_{\theta\phi}(\theta) = \langle u'_\theta(\theta, \phi) u'_\phi(\theta, \phi) \rangle = K^2 s_1^2 \Re \{ v_\theta^*(\theta) v_\phi(\theta) \} / 2 \quad (6)$$

where the angular brackets denote a longitudinal average.

### 3. Results

Figure 1 shows the obtained velocity eigenfunctions of the  $m = 1$  high-latitude mode, which has a large longitudinal velocity of  $\approx 13$  m/s above  $60^\circ$  and shows a spiral pattern around the poles. The bottom panel of figure 1 shows the computed horizontal Reynolds

stress  $Q_{\theta\phi}$  of the  $m = 1$  high-latitude mode, which is positive (negative) in the northern (southern) hemisphere, indicating equatorward transport of angular momentum. Hathaway and Upton (2021, their figure 7) reported a similar latitudinal profile.

For this mode, the Reynolds stress,  $Q_{\theta\phi}$  has a peak value of about  $38 \text{ m}^2/\text{s}^2$ , which it attains above latitude  $70^\circ$ . To understand the cause of these Reynolds stresses, we use the solar differential rotation data (Larson and Schou 2018) to compute the critical latitudes  $\lambda_{\text{crit}}$ . The locations of the critical latitudes ( $\lambda_{\text{crit}} = \pm 58^\circ$  for the  $m = 1$  high-latitude mode) are shown by green dotted lines in Fig. 1. We note that most of the non-zero  $Q_{\theta\phi}$  is found above the critical latitude  $\lambda_{\text{crit}}$ .

We also compute the Reynolds stress focusing only on the quiet Sun period (Jan 2017 - Dec 2020) during which this mode has a much higher amplitudes. The angular momentum transported by the  $m = 1$  high-latitude mode is much more significant during the quiet Sun period, see the red curve in Fig. 1. The importance of the contribution of the  $m = 1$  high-latitude mode to the overall angular momentum balance is discussed in an upcoming paper by Bekki *et al.* (2024).

## Acknowledgements

We thank Z.-C. Liang and D. Fournier for helpful discussions. The HMI data are courtesy of NASA/SDO and the HMI Science team. Y.M. acknowledges support from the International Max-Planck Research School (IMPRS) for Solar System Science at the University of Göttingen. We acknowledge support from ERC Synergy Grant WHOLESUN 81218 and Deutsche Forschungsgemeinschaft (DFG, German Research Foundation) through SFB 1456/432680300 Mathematics of Experiment, project C04.

## References

- Basu, S., Antia, H. M., & Tripathy, S. C. 1999, Ring Diagram Analysis of Near-Surface Flows in the Sun. *ApJ*, 512, 458–470.
- Bekki, Y., Cameron, R. H., & Gizon, L. 2022a, Theory of solar oscillations in the inertial frequency range: Linear modes of the convection zone. *A&A*, 662, A16.
- Bekki, Y., Cameron, R. H., & Gizon, L. 2022b, Theory of solar oscillations in the inertial frequency range: Amplitudes of equatorial modes from a nonlinear rotating convection simulation. *A&A*, 666, A135.
- Bekki, Y., Cameron, R. H., & Gizon, L. 2024, The Sun's differential rotation is controlled by baroclinically unstable high-latitude inertial modes. *Science Adv.*, under review.
- Bogart, R. S., Baldner, C., Basu, S., Haber, D. A., & Rabello-Soares, M. C. HMI ring diagram analysis I. The processing pipeline. In *GONG-SoHO 24: A New Era of Seismology of the Sun and Solar-Like Stars 2011*, Vol. 271 of *J. Phys. Conf. Series*, 012008.
- Bogart, R. S., Baldner, C., Basu, S., Haber, D. A., & Rabello-Soares, M. C. HMI ring diagram analysis II. Data products. In *GONG-SoHO 24: A New Era of Seismology of the Sun and Solar-Like Stars 2011*, Vol. 271, *J. Phys. Conf. Series*, 012009.
- Bogart, R. S., Baldner, C. S., & Basu, S. 2015, Evolution of Near-surface Flows Inferred from High-resolution Ring-diagram Analysis. *ApJ*, 807, 125.
- Fournier, D., Gizon, L., & Hysted, L. 2022, Viscous inertial modes on a differentially rotating sphere: Comparison with solar observations. *A&A*, 664, A6.
- Gizon, L., Cameron, R. H., Bekki, Y., Birch, A. C., Bogart, R. S., Brun, A. S., Damiani, C., Fournier, D., Hysted, L., Jain, K., Lekshmi, B., Liang, Z.-C., & Proxauf, B. 2021, Solar inertial modes: Observations, identification, and diagnostic promise. *A&A*, 652, L6.
- Gizon, L., Fournier, D., & Albekioni, M. 2020, Effect of latitudinal differential rotation on solar Rossby waves: Critical layers, eigenfunctions, and momentum fluxes in the equatorial  $\beta$  plane. *A&A*, 642, A178.
- Hanson, C. S., Hanasoge, S., & Sreenivasan, K. R. 2022, Discovery of high-frequency retrograde vorticity waves in the Sun. *Nature Astron.*, 6, 708–714.

- Hathaway, D. H. & Upton, L. A. 2021, Hydrodynamic Properties of the Sun's Giant Cellular Flows. *ApJ*, 908, 160.
- Hill, F. 1988, Rings and Trumpets—Three-dimensional Power Spectra of Solar Oscillations. *ApJ*, 333, 996.
- Larson, T. P. & Schou, J. 2018, Global-Mode Analysis of Full-Disk Data from the Michelson Doppler Imager and the Helioseismic and Magnetic Imager. *Solar Phys.*, 293, 29.
- Löptien, B., Gizon, L., Birch, A. C., Schou, J., Proxauf, B., Duvall, T. L., Bogart, R. S., & Christensen, U. R. 2018, Global-scale equatorial Rossby waves as an essential component of solar internal dynamics. *Nature Astron.*, 2, 568–573.